Electrically continuous graphene from single crystal copper verified by terahertz conductance spectroscopy and micro four-point probe.

Buron, Jonas Christian Due; Pizzocchero, Filippo; Jessen, Bjarke Sørensen; Booth, Tim ; Nielsen, Peter F.; Hansen, Ole; Hilke, Michael; Whiteway, Eric; Jepsen, Peter Uhd; Bøggild, Peter; Petersen, Dirch Hjorth

Published in:
Nano Letters

Link to article, DOI:
10.1021/nl5028167

Publication date:
2014

Document Version
Peer reviewed version

Electrically continuous graphene from single crystal copper verified by terahertz conductance spectroscopy and micro four-point probe

Jonas D. Buron[†,‡], *Filippo Pizzocchero*[†], *Bjarke S. Jessen*[†,§], *Timothy J. Booth*[†], *Peter F. Nielsen*[ǀ], *Ole Hansen*[†,¤], *Michael Hilke*[#], *Eric Whiteway*[#], *Peter U. Jepsen*[‡], *Peter Bøggild*[†,§] , *Dirch H. Petersen*[†]

†DTU Nanotech, Technical University of Denmark, Ørsteds Plads 345E, Kgs. Lyngby, 2800 Denmark,

[§] Center for Nanostructured Graphene (CNG), Technical University of Denmark, Ørsteds Plads , Kgs. Lyngby, 2800 Denmark

‡ DTU Fotonik, Technical University of Denmark, Ørsteds Plads 343, Kgs. Lyngby, 2800 Denmark

[ǀ] Capres A/S, Diplomvej, Building 373, Kgs. Lyngby, 2800 Denmark

[#] Department of Physics, McGill University, Montréal, Québec, Canada H3A 2T8, McGill University

¤ Center for Individual Nanoparticle Functionality (CINF), Technical University of Denmark, Building 345E, Kgs. Lyngby, 2800 Denmark

* Corresponding author: dirch.petersen@nanotech.dtu.dk

** *Jonas D. Buron, Filippo Pizzocchero and Dirch H Petersen contributed equally to the work.*

mailto:peter.boggild@nanotech.dtu.dk

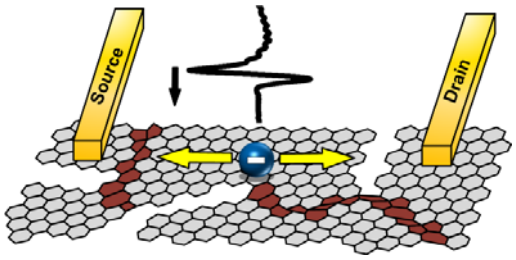

Abstract

The electrical performance of graphene synthesized by chemical vapour deposition and transferred to insulating surfaces may be compromised by extended defects, including for instance grain boundaries, cracks, wrinkles and tears. In this study we experimentally investigate and compare the nano- and micro-scale electrical continuity, after transfer to SiO_2 surfaces, of single layer graphene grown on cm-size single crystal copper with that of previously studied graphene films, grown on commercially available copper foil. The electrical continuity of the graphene films is analysed using two non-invasive conductance characterization methods: ultra-broadband terahertz time-domain spectroscopy and micro four-point probe, which probe the electrical properties of the graphene film on different length scales; 100 nm and 10 µm, respectively. Ultra-broadband terahertz time-domain spectroscopy allows for measurement of the complex conductance response in the frequency range 1-15 terahertz, covering the entire intraband conductance spectrum, and reveals that the conductance response for the graphene grown on single crystalline copper intimately follows the Drude model for a barrier-free conductor. In contrast, the graphene grown on commercial foil copper shows a distinctly non-Drude conductance spectrum that is better described by the Drude-Smith model, which incorporates the effect of preferential carrier backscattering associated with extended, electronic barriers with a typical separation on the order of 100 nm. Micro four-point probe resistance values measured on graphene grown on single crystalline copper in two different voltage-current configurations show close agreement with the expected distributions for a continuous 2D conductor, in contrast with previous observations on graphene grown on commercial copper foil. The terahertz and micro four-point probe conductance values of the graphene grown on single crystalline copper shows a close to unity correlation, in contrast with those of the graphene grown on commercial copper foil, which we explain by the absence of extended defects on the microscale in CVD graphene grown on single crystalline copper. The presented results demonstrate that the graphene grown on single crystal copper is electrically continuous on the nano-, micro-, as well as intermediate scales.

Keywords: THz-TDS, M4PP, transport, defect, large-scale, thin film, metrology, correlation

Introduction

Since the isolation of single layer graphene by micromechanical exfoliation[1], synthesis processes such as chemical vapour deposition (CVD) on nickel[2] and copper[3] (Cu) have been intensively studied to provide a route towards fabrication of graphene of quality similar to that of exfoliated graphene on a scale relevant for systematic research, prototyping and commercial applications. Since electronic mean free path[4], carrier mobility and electrical continuity[5–10] are defining parameters for electronic device performance[11], the ability to reproducibly fabricate, transfer and verify graphene of high electronic quality is a prerequisite for applications within electronics. Several groups reported that the quality of CVD graphene catalysed on Cu substrates depends strongly on the crystal orientation of the Cu, with growth on the Cu(111) facet leading to the highest quality of graphene[12–14]. In continuation of this research, we grow graphene on Cu(111) single crystals (SC), similar to earlier reports[15]. The use of expensive SC metallic substrates suggests application of a transfer method that avoids etching of the substrate. To this end we employ the approach of

electrochemical delamination described by Wang et al.[16] We modified the technique for higher areal coverage and lower number of tears and cracks by control of the electrode potential.

Electrical properties of CVD graphene can be severely degraded by the presence of extended (line-shaped) defects, such as grain boundaries, cracks and wrinkles, which can lead to non-continuous electrical conduction on a multitude of length scales. The influence of such extended defects is likely to lead to erroneous evaluation of sheet resistance and mobility in standard hall bar device measurements if their characteristic length is on the order of device dimensions. For sufficiently high densities, extended barriers in thin graphene films can lead to electrical behaviour similar to that found in two dimensional sub-critical or critical percolation networks[6,17,18], where electronic transport on scales similar to or larger than the inter-barrier distance is severely impeded. Evaluation of electrical continuity from nanoscopic to microscopic scales is therefore of particular relevance for implementation of graphene in micro- and nano-electronics.

In a prior study[19] we used dual configuration micro four-point probe (M4PP) measurements and terahertz time-domain spectroscopy (THz-TDS) to evaluate electrical continuity of graphene on micro- and nanometer length scales. The graphene films investigated in that study showed traits of electrical discontinuity on micrometer scales, resulting in a poor correlation between nanoscopic and microscopic conductance. Our previous investigation could, however, not discern the details of nanoscopic conduction dynamics and electrical continuity, owing to limitations in the bandwidth of THz-TDS measurements.

In this paper we investigate and compare the electrical continuity of CVD graphene films grown on SC Cu and commercial foil (CF) Cu using two independent, non-invasive, spatially resolved techniques: THz-TDS and scanning M4PP[19]. The methods probe the conductance and electrical continuity on different lengths scales of approximately 100 nm and 10 μm, respectively. Through observation of distinct Drude and Drude-Smith[20–23] conductance spectra in CVD graphene films grown on SC Cu and CF Cu, respectively, ultra-broadband THz-TDS can distinguish the response of electrically continuous graphene from that of graphene with extended defects on the 100 nm scale. While the current observation of Drude conduction dynamics in graphene grown on SC Cu is in agreement with a number of previous observations in conventional THz-TDS studies of high quality, large area graphene films[24–28], the presented Drude-Smith response from graphene grown on CF Cu is to our knowledge the first definitive observation of a non-Drude static terahertz conductance response from graphene. Analogously, dual configuration M4PP measurements allow for evaluation of two-dimensional continuity on the 10 μm scale. Where our previous study revealed discontinuity through observation of electrical behaviour deviating from that of an infinite conducting sheet,[6,19] we here confirm microscopic, electrical continuity of SC Cu grown large scale CVD graphene. Finally, we verify electrical continuity on intermediate length scales through observation of highly correlated nanoscopic and microscopic sheet conductances of the investigated graphene grown on SC Cu.

Materials and Methods

Growth and transfer of single crystal copper grown graphene

Graphene was grown on 10x10x1 mm^3 single crystal Cu(111) (MTI Corporation, uncertainty 2°, purity higher than 99.9999%, initial roughness lower than 30 Å). The substrate was initially annealed for 3 hours at

1040°C in a mixed H2 (1000 sccm)/Ar (200 sccm) atmosphere at 3 mbar. The H_2 flow was then reduced to 300 sccm, and the pressure to 1.5 mbar. The graphene was grown by introducing methane precursor (2 sccm) for 10 minutes. The sample was then cooled down to room temperature in pure Ar flow (1000 sccm). To transfer the graphene in a manner that allows reuse of the Cu substrate while still preserving the integrity of the graphene, an electrochemical delamination transfer based on the approach described by Wang et al[16] was used. The technique was however modified for a gentler and slower release of the graphene film by limiting the electrode potential, which we find results in a slower delamination, with higher coverage on the target substrate. The SC Cu grown graphene was transferred to high resistivity (> 10.000 Ωcm) silicon (HR-Si) covered with 90 nm SiO_2.

Coverage analysis

To make a quantitative assessment of the graphene coverage, a grid of 210 images were acquired automatically using a Nikon Eclipse L200 microscope equipped with a high-precision Prior Scientific motorized stage and saved with a resolution of ~0.48 µm/pixel. The images were subsequently stitched into a single high-resolution image and analysed. Areas with single layer graphene were identified and measured by convoluting the spectral contrast of graphene[29] with the spectral sensitivity of the CCD sensor to obtain RGB values for the contrast.

Micro Raman spectroscopy

Micro Raman spectroscopy measurements were carried out using a Thermo Fisher Scientific DXR Raman microscope using a 433 nm (blue) excitation laser with a power of 1 mW and a spot size of around 1 µm. The graphene was first measured in 1600 locations with 125 µm spacing on the surface of the SC Cu substrate after growth, and repeated on the transferred graphene film.

Terahertz time-domain spectroscopy

THz-TDS was performed with two separate spectrometers; one for ultra-broadband, single position THz-TDS, and one for spatially scanned conventional THz-TDS. The ultra-broadband THz time-domain spectrometer is based on THz generation in a two-color laser induced air plasma[30–32] and THz detection by air biased coherent detection[33,34]. This approach produces THz pulses with a bandwidth up to 40 THz, close to that of the 35 fs optical pulses used for generation and detection, and facilitated spectroscopy on the present samples in a range from 1-15 THz. Further details on the ultra-broadband THz-TDS setup are described previously[23,35,36]. Due to relatively large phase shifts associated with small variations in substrate thickness from sample position to reference position at multi-THz frequencies, it was necessary to correct the phase of the measured ultra-broadband THz-TDS data accordingly. This commonly used procedure was first introduced by Jeon et al[37].

Conventional scanned THz-TDS from 0.1-1.5 THz is performed using a commercial fiber-coupled spectrometer, also described in detail elsewhere[19]. The sample is scanned in the THz focal plane between fiber coupled emitter and detector units to form sheet conductance line scans and sheet conductance maps with 350 µm spatial resolution (at 1 THz).

For both conventional and ultra-broadband THz-TDS measurements, the sheet conductance of the graphene films, $\sigma_s(f)$, is extracted as described in Ref[19], by relating the Fourier transform, $\tilde{E}_{sub}(f)$, of a reference THz waveform transmitted through the non-graphene-covered HR-Si substrate with n_{Si}=3.417[29,30] to the Fourier transform, $\tilde{E}_{sub+graphene}(f)$, of a sample THz waveform transmitted through the graphene-covered HR-Si

substrate. Since the THz radiation interacts strongly with the free carriers in the graphene film, the complex transmission function, $\tilde{T}_{film}(f) = \tilde{E}_{sub+graphene}(f)/\tilde{E}_{sub}(f)$, can be related to the sheet conductance of the graphene film through the Fresnel coefficients for transmission and reflection at the boundaries in the sample structure. For the directly transmitted pulse and the 1st round-trip echo the relations are given by equation (1) and (2), respectively.

$$\tilde{\sigma}_{s,1st\ Pulse}(f) = \frac{1}{Z_0}\frac{n_A}{\tilde{T}_{film}(f)} - n_A, \tag{1}$$

$$\tilde{\sigma}_{s,2nd\ Pulse}(f) = \frac{\pm n_A\sqrt{{n_A}^2 + 4n_A n_B \tilde{T}_{film}(f)} - \tilde{n}_A{}^2 - 2n_A {n_B}^2 \tilde{T}_{film}(f)}{2n_B Z_0 \tilde{T}_{film}(f)}, \tag{2}$$

where $n_A = n_{Si} + 1$ and $n_B = n_{Si} - 1$, f is the frequency, and Z_0=377 Ω is the vacuum impedance. For the graphene film grown on SC Cu, $\sigma_s(f)$ is determined from an analysis of THz waveforms transmitted directly through the sample (1st pulse). For the graphene film grown on CF Cu, $\sigma_s(f)$ is determined from the 1st echo pulse (2nd pulse), resulting from two internal reflections in the sample. Using the 1st echo pulse increases the contrast between reference and sample measurements and works to improve the overall signal-to-noise ratio of the measurement for graphene films with a small THz response.

Dual configuration micro-four point measurement (M4PP)

Sheet conductance, σ_s, was mapped using Au coated micro four-point probes with three-way flexible electrodes[38,39] on a CAPRES MicroRSP-M150 system. The modified van der Pauw equation[40]

$$e^{2\pi R_A \sigma_s} - e^{2\pi R_B \sigma_s} = 1, \tag{3}$$

is solved to extract σ_s from two electrode configurations, in which the current and voltage electrodes are switched to measure resistances $R_A = V_{23}/I_{14}$, and $R_B = V_{24}/I_{13}$ (cf. figure 3). Using this method, in-line electrode position errors are eliminated and geometrical confinement errors reduced in the evaluation of σ_s, as demonstrated for small samples[41]. Whereas evenly distributed defects much smaller than the electrode pitch may contribute by reducing the average sheet conductance,[42] interior defects on the scale of the electrode pitch result in incorrigible errors[43] as the measurement sensitivity to defects become non-linear for strong and finite area (or length) perturbations of the local sheet conductance.[44] The latter type of defect, results in measured R_A/R_B ratios which differ from that predicted for an infinite conducting sheet, R_A/R_B=ln(4)/ln(3), and may be used in evaluation of electrical continuity of the measured film. The graphene samples were measured using multi-electrode probes (see Fig 3a) for concurrent measurements with multiple equidistant electrode pitches of 4 μm, 8 μm and 12 μm, and a set current of 5 μA was chosen in order to avoid current induced sample damage[45].

Results and Discussion

CVD graphene grown on Cu (111) single crystal was transferred by electrochemical delamination[16] to SiO_2 grown on HR Si wafer. The average coverage in the total 1 x 1 cm^2 transferred area is ~92%, and reaches 99% in several ~4 mm^2 regions. This is concluded from stitched high resolution optical images (figure 1a),

collected across the sample and analyzed in terms of their optical contrast. Each pixel in the generated coverage map (figure 1b) indicates the presence/absence of graphene as bright/dark color, respectively.

As shown in figure 1c, the Raman response of the transferred graphene film exhibits distinct signatures of monolayer graphene with single-peaked G and 2D bands. The lattice defect density in the graphene film is monitored via the I(D)/I(G) peak intensity ratio of the Raman D and G peaks[46–48]. Before transfer the average I(D)/I(G) peak intensity ratio from 1600 measurements on the as-grown graphene film on SC Cu was 0.07±0.03, which after transfer increased to a value of 0.15±0.07.

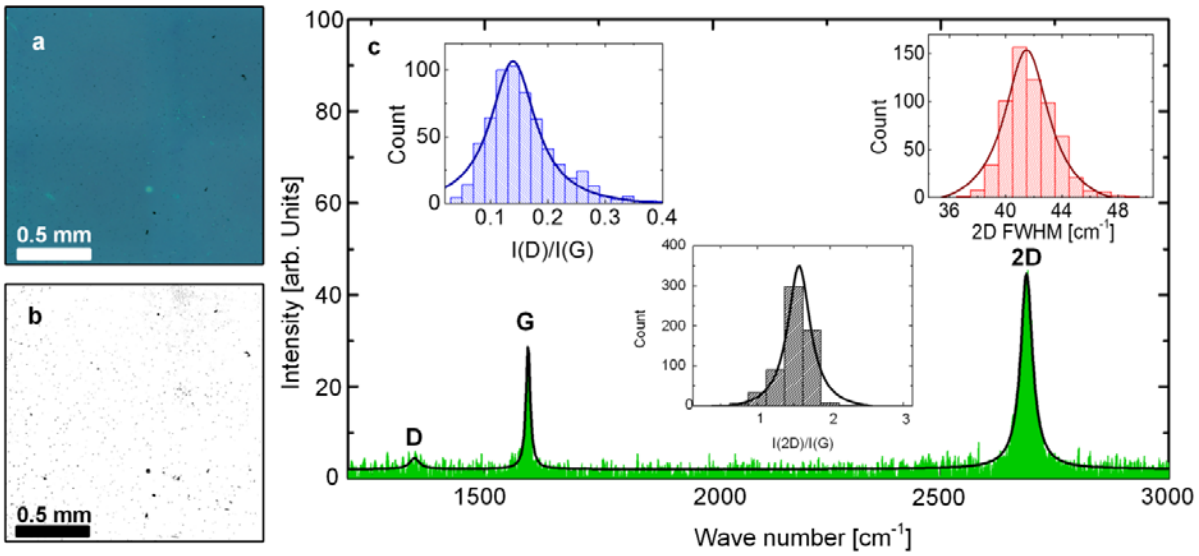

Figure 1 – (a) Optical image of the graphene film on the silicon dioxide surface. **(b)** Coverage map with bright areas indicating regions that have the optical contrast signature of single layer graphene[29]. The total coverage is 99%. **(c)** Raman spectrum of the transferred graphene film exhibits monolayer graphene response. Shown is also single Lorentzian fits to D, G and 2D peaks. Insets: Distribution of I(D)/I(G) and I(2D)/I(G) ratios as well as FWHM(2D) after transfer process.

Nanoscale electrical continuity: terahertz time-domain conductance spectroscopy

The nanoscale electrical conductance and continuity of the graphene films investigated with ultra-broadband THz-TDS, in the frequency range 1-15 THz, as well as conventional scanning THz-TDS in the 0.1-1.5 THz frequency range.

Figures 2a-b show time-domain waveforms for graphene grown on SC Cu and CF Cu obtained with ultra-broadband THz-TDS, while the corresponding waveforms obtained with conventional THz-TDS are shown as inserts. The real and imaginary parts of the extracted sheet conductance are shown in figs. 2c and 2d. The conductance spectrum observed with conventional THz-TDS for the SC Cu grown graphene film (open markers in fig. 2c) shows real and imaginary parts of the conductance that slowly decreases with frequency and slowly increases with frequency, respectively. This type of conductance spectrum is characteristic of a Drude conductor, for which charge carriers move unhindered between isotropic point scattering events with the scattering rate $\Gamma=1/\tau$[19,25,26]. The ultra-broadband THz-TDS conductance spectrum (filled markers in fig. 2c) agrees and overlaps with conventional THz-TDS data at low frequencies, allowing accurate fitting of the Drude model with scattering time τ = 68±3 fs, and σ_{DC} = 2.19±0.026 mS. All prominent features of the Drude spectrum are resolved, including the crossover of real and imaginary sheet conductance. While the SC Cu grown graphene film thus possesses the electrical characteristics of a continuous conductor one important question is: at which scale? Under the assumption of diffusive carrier transport dominated by long-range

charged impurity scattering, the carrier density N, mobility μ, and characteristic transport length scale of an ac conductance measurement, L_{THz}, can be evaluated from the measured τ and σ_{DC}, following the procedures of[49–52]

$$N = \frac{\pi\hbar^2}{e^4 {v_F}^2} \frac{{\sigma_{DC}}^2}{\tau^2} = (5.45 \pm 0.61) \times 10^{12} \text{ cm}^{-2}, \tag{4}$$

$$\mu = \frac{\sigma_{DC}}{eN} = (2506 \pm 251) \ \frac{\text{cm}^2}{\text{Vs}}, \tag{5}$$

$$L_{THz} = \sqrt{\frac{D}{2\pi f}}. \tag{6}$$

where $D = \frac{E_F \sigma_s}{2Ne^2}$ is the carrier diffusivity and $v_F = 10^6$ m/s is used for the Fermi velocity[51]. The experimental frequency range of 0.1-10.0 THz corresponds to a characteristic transport length scale from 250 nm to 20 nm. The observed Drude conductance spectrum can thus be interpreted as a signature of electronic continuity on nano- to sub-micron-scale. Furthermore, the measured scattering time can be used to evaluate the mean free path of carriers:

$$l_{mfp} = v_F \tau = (68 \pm 3) \text{ nm}. \tag{7}$$

The conductance spectrum that we observe for the CF Cu grown graphene shows real and imaginary parts of the conductance that are predominantly flat and constant in the lower frequency range resolved by conventional THz-TDS (open markers in fig. 2d). While this flat conductance spectrum could be accounted for by a Drude response with a scattering rate much larger than the accessible frequency range ($2\pi f \ll \Gamma$) of conventional THz-TDS, ultra-broadband THz-TDS investigations shows that the conductance response for the CF Cu grown graphene film differs fundamentally from the Drude model (filled markers in fig. 2d). This is exemplified in figure 2b by a Drude model best fit with τ=10 fs and σ_{DC}=0.74 mS shown in grey lines. The two techniques agree very well at low frequencies, but the ultra-broadband conductance spectrum reveals that the flat low-frequency conductance spectrum is not a signature of a pure Drude conductance response. The conductance spectrum shows a slight, but distinct suppression of the real conductance from DC to around 2 THz, accompanied by a flat, diminishing or even slightly negative imaginary conductance in the same region. A previous conventional THz-TDS investigation indicated a similar response from CVD graphene[53]. These features are representative of a capacitive response and cannot be reproduced by the Drude model. They represent to our knowledge the first definitive observation of a non-Drude static terahertz conductance response from graphene where all features in the intraband conductance response are resolved. Similar conductance spectra have commonly been observed in e.g. nano-disordered systems such as semiconductor nano-crystal systems and conjugated polymer systems. In these studies the phenomenological Drude-Smith model has been shown to provide a simple, but natural extension to the Drude model, capable of describing the conductance response of solid state systems with some degree of carrier localization[20–23,54]. The Drude-Smith model is expressed as

$$\tilde{\sigma}(f) = \frac{W_D}{1 - i2\pi f\tau} \left[1 + \sum_{n=1}^{\infty} \frac{c_n}{(1 - i2\pi f\tau)^n} \right], \tag{8}$$

where W_D is the Drude weight, τ is the momentum relaxation time, and c_n are so-called backscattering parameters, which are a measure of the persistence of velocity upon carrier scattering[21,22,54].

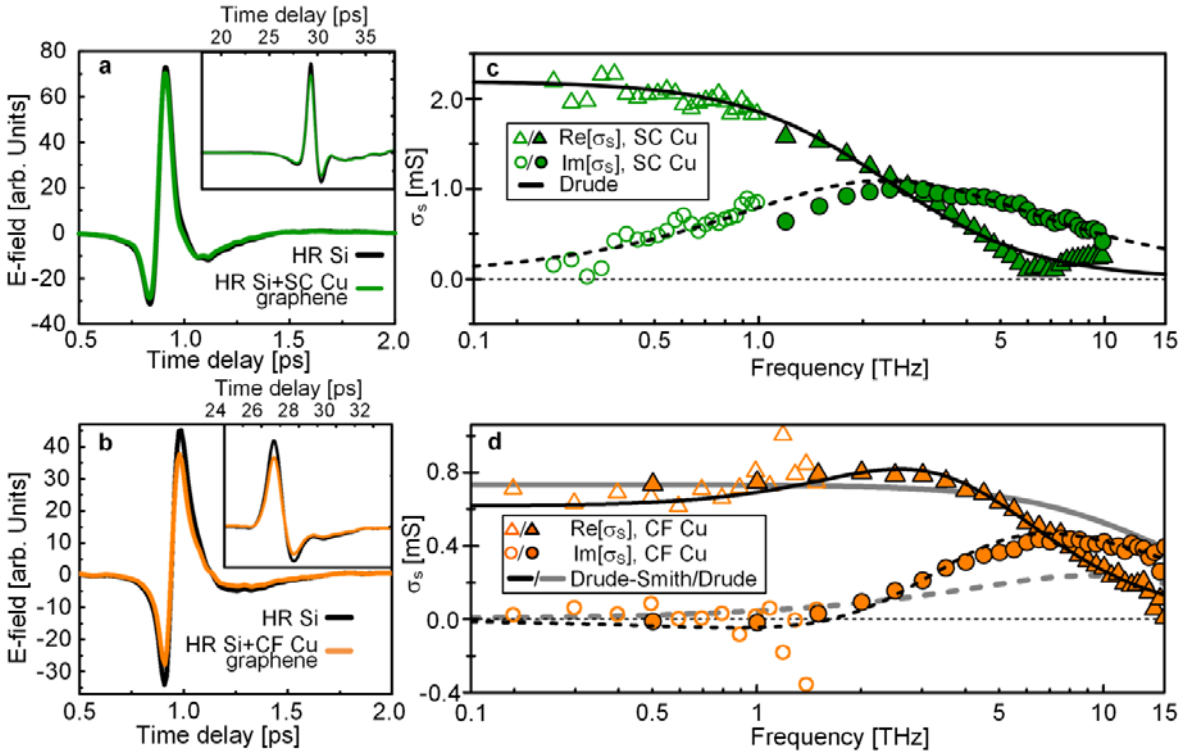

Figure 2. **(a,b)** THz-TDS time-domain waveforms for ultra-broadband THz pulses transmitted through clean HR-Si substrate (black curves), SC Cu grown graphene on HR-Si (green curve), and CF Cu grown graphene on HR-Si (orange curve). THz-TDS experiments are based on the directly transmitted pulse for SC Cu grown graphene and the first echo pulse for CF Cu grown graphene to optimize the S/N of the measurement, see Methods section for more details. Insets show the corresponding conventional THz-TDS measurements of the same samples. **(c,d)** Real (triangles) and imaginary (circles) conductance spectra obtained from ultra-broadband (filled) and conventional (empty) THz-TDS measurements. Black/grey curves represents real (full lines) and imaginary (dashed lines) parts, respectively, of fitted Drude (SCC-grown graphene) and Drude-Smith (CF-grown graphene) model.

In the Drude-Smith framework, a suppression of DC and low frequency conductance as well as a negative low frequency, imaginary conductance, such as in our present observations, arise as a consequence of charge carrier localization caused by preferential carrier backscattering on extended electronic barriers on a nanoscopic length scale smaller than or similar to the mean free path of the charge carriers in the system[18]. Such preferential carrier backscattering is modelled in the Drude-Smith framework by statistically retaining a fraction of the initial momentum vector of carriers upon scattering events, parameterized by the set of c_n coefficients. In the current impulse response formalism, the c_n parameters can be shown to be the Taylor coefficients of an arbitrary pertubation function, $g(t/\tau)$, describing the deviations of the Drude-Smith impulse response from the exponentially decaying Drude impulse response as $j(t) = g(t/\tau)\mathrm{e}^{-t/\tau}$. By including only the first term in the series and omitting the subscript *n*, we are thus including only the first-order correction to the Drude conductance response caused by preferential carrier backscattering[22,23]. In this truncated expression, a single parameter, *c*, describes the degree of preferential carrier backscattering, where *c*=0 corresponds to complete momentum randomization upon scattering, recovering the Drude model, while *c* = -1 accounts for full momentum reversal, leading to complete backscattering of carriers in all scattering events. Recent Monte Carlo carrier trajectory simulations[55] found the conductance response of nanocrystal

arrays with semi-reflecting boundaries to be well described by the Drude-Smith model, where a phenomenological correspondence between c and barrier reflectivity was found for systems with crystal dimensions comparable to the bulk mean free path[56]. As seen from figure 2d, we find the measured sheet conductance response to be well described by the Drude-Smith model with a Drude weight W_D = 1.54 mS, a momentum relaxation time τ = 43 fs, a backscattering parameter c = -0.60, and a DC sheet conductance of $\sigma_{DC}=W_D(1+c)$=0.62 mS, and we therefore suggest an interpretation of the measured conductance spectrum for the CF Cu grown graphene film in a picture analogous to previous studies of nano-disordered solid state systems[20–23,54]. Our observations thus suggest the existence of extended, partially reflecting barriers for electronic transport in the graphene film grown on CF Cu with a characteristic length scale similar to the mean free path of the system, given as

$$l_{mfp} = v_F \tau = 43 \text{ nm} \tag{9}$$

Likely origins of such defects on this length scale in CVD graphene films include crystal domain boundaries and incomplete growth coverage, while transfer-related damages such as e.g. rips or ripples will typically dominate on larger length scales. Furthermore, a value of c = -0.60 seems to indicate partially transmitting barriers[21,55], which points more towards grain boundaries and wrinkles, rather than fully insulating defects such as rips and tears. An interpretation within the Drude-Smith picture of nanoscopically localized carriers thus suggests that the observed non-Drude conductance features are a signature of restricted movement of carriers due to preferential backscattering on graphene grain boundaries[7] or ripples in the poly-crystalline CVD graphene film.

Microscale electrical continuity: dual configuration micro four-point measurements

As a complementary method dual configuration M4PP measurements allows electrical continuity analysis of the graphene film on the microscopic scale given by the probe pitch[19], through comparison of two different current-voltage configurations, termed A and B (see Figure 3). In the ideal case of measurements with perfectly equidistant co-linear electrodes on a perfectly two-dimensional conductor, the ratio R_A/R_B of the measured resistances is exactly $\ln(4)/\ln(3) \approx 1.26$[19]. In the more realistic case of Gaussian distributed positions of the four electrode contacts (due to positioning uncertainty), a perfectly two-dimensional conductor instead gives rise to a distinct statistical distribution of measured R_A/R_B ratios centered near 1.26. These distributions, obtained by Monte Carlo simulations of a two-dimensional electrically continuous film,[19] are shown in Figure 3. Here, normal distributed electrode position errors were applied to each electrode in analytical Monte Carlo simulations to predict the distribution of R_A/R_B ratios as function of electrode pitch. A normal distributed electrode position error of 0.4 µm was found from the relative standard deviation of A-configuration measurements; a methodology we presented in ref [38], and which is consistent with the equivalent analysis for B-configurations and variable electrode pitch. Note that an independent measurement of the magnitude of electrode position errors does not exist for measurements on ideal graphene. In the case of insulating defects close to the probes, the R_A/R_B ratio converges towards 1, which we previously associated with 1D-like or percolative transport[6,19]. This dual configuration measurement strategy thus offers insight into the degree of microscale spatial electrical continuity of the film, independently from the absolute value of the conductance, which is not immediately possible from a conventional single-configuration conductance measurement.

Dual configuration M4PP measurements were performed across the transferred SC Cu grown graphene film using multi-electrode probes for concurrent measurements with equidistant electrode pitches of 4 µm, 8 µm and 12 µm (see figure 3a).

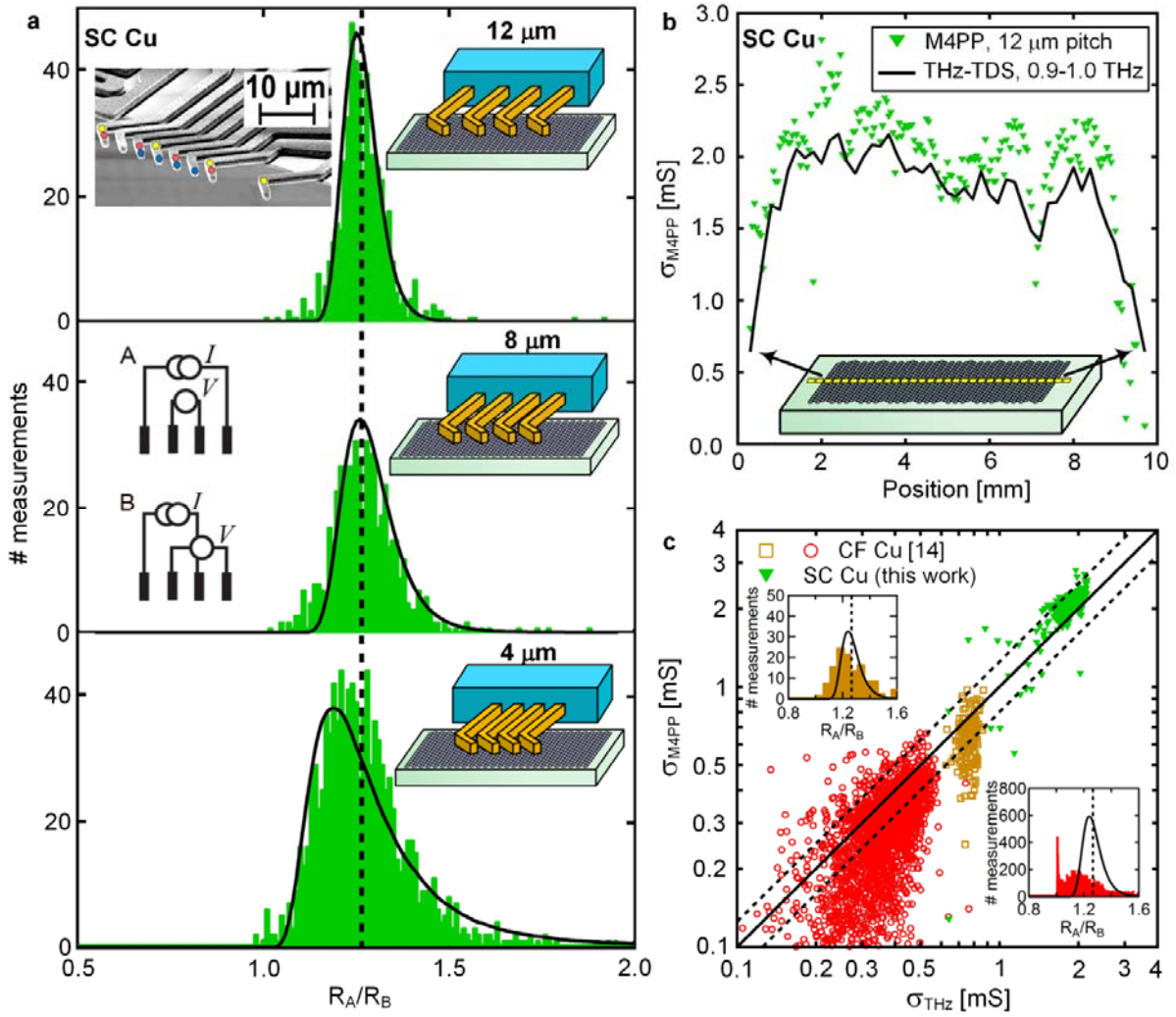

Figure 3. **a)** Histograms of R_A/R_B ratio distributions for graphene grown on SC Cu, using electrode pitch of 12 µm, 8 µm and 4 µm, respectively. In contrast with graphene grown on CF Cu investigated in previous work, the distributions of the R_A/R_B ratios follow the Monte Carlo prediction for an ideal 2D conductor with a Gaussian probe position error of 400 nm. A scanning electron micrograph of a multipoint microprobe (adapted from Ref [57]) as well as the A and B configurations are illustrated as insets. The colored circles illustrate how 4 µm pitch (red) and 8 µm pitch (green) measurements can be carried out by multiplexing current and voltage connections during a single probe-sample engagement. **(b)** THz-TDS and M4PP conductance line scan across the graphene grown on and transferred from SC Cu, with the measured sample shown as an inset. The two conductance sets are spatially well correlated across the 8 mm, with a small overshoot of the M4PP measurements. **(c)** Correlation plot of THz-TDS and M4PP conductance values, with the dashed lines indicating 125% and 80% with respect to the 1:1 correlation (full line). For the previously investigated graphene films grown on CF Cu, a large portion of the M4PP conductance values are significantly lower than the 80% correlation line. The current study of graphene grown on SC Cu shows that 79% of the M4PP data points lie within 100% and 125% lines compared to the THz measurement values.

We observe a mean difference in the spatially correlated sheet conductance of less than 4 % between the three different electrode pitches and Pearson correlation values of R^2=0.932, R^2=0.884 and R^2=0.951, when comparing 4 µm with 8 µm, 4 µm with 12 µm and 8 µm with 12 µm, respectively. From this we conclude that the measured sheet conductance is in this case independent on electrode pitch. In addition, the obtained

R_A/R_B ratios follow the predicted distribution functions for M4PP measurements on an infinite, continuous, 2-dimensional conducting sheet for all three electrode pitches used, although with minor unexplained deviations for the smallest electrode pitch of 4 μm, which could be related to the finite contact size. In our previous study, two CVD graphene films grown on CF Cu were investigated in a similar manner, although here with a probe pitch of 10 μm, see reference[19]. Both graphene films show broader R_A/R_B distributions (cf. inserts figure 3c), with especially the distribution of one graphene film exhibiting a distinct clustering of values at exactly R_A/R_B = 1.00. While the R_A/R_B ratio distribution for one of the previously investigated graphene films grown on CF Cu qualitatively resembles a 2-dimensional conductor with some additional broadening, the distribution for the second graphene film clearly differs. Figure 3b compares spatially the THz-TDS conductance averaged in the frequency range of 0.9-1.0 THz (spot size approx. 350 μm) to M4PP conductance obtained using 12 μm pitch. The M4PP σ_s values are generally 10-25% higher and show larger spatial variations in good agreement with the expected behaviour for a smaller spot size[57]. In figure 3c, σ_s measured with M4PP and THz-TDS are compared for each spatial position, and for reference we include correlation results for the CF Cu graphene previously published[19]. For the SC Cu grown graphene, 79% of all the $\sigma_{s,M4PP}$ values lie within 100% and 125% (dashed lines in figure 3c) of the $\sigma_{s,THz}$ values extracted for the same area with a relatively small spread, primarily along the direction of 1:1 correlation. This suggests the presence of spatial features in the electrical properties of the film that affect M4PP and THz conductance in a similar manner, such as e.g. spatial variations in mobility and/or doping of the graphene film. The systematically lower THz conductance can be ascribed to the fact that we compare the conductance at 0.9-1.0 THz to the DC sheet conductance measured by M4PP. As seen in Fig 2, the real part of the conductance decreases approximately 18% from 2.19 mS to 1.85 mS in the frequency range from 0.1 THz to 1.0 THz, which corresponds roughly to the generally observed difference of 10-25%. Because the THz-TDS spot size increases from 0.35 mm to 3 mm from 1 THz to 0.1 THz, it is not possible to correct for this error while maintaining spatial resolution to compare the M4PP and the THz-TDS as in Fig 3b-c. In contrast only 53% and 35% of the points previously measured on graphene films grown on CF Cu lie within the 80%-125% range, with significantly larger spread towards low values on values obtained by M4PP than by THz-TDS, resulting in a large fraction of the M4PP sheet conductance values being up to 5-10 times smaller than their THz-TDS counterparts.

The strong correlation between nanoscale (THz-TDS) and microscale (M4PP) sheet conductance of the CVD graphene grown on SC Cu (figure 3b-c) suggests that this film, in contrast with the investigated graphene grown on CF Cu, has a negligible number of extended defects with characteristic length scales between the characteristic transport length scale of the THz-TDS (20-250 nm) and the electrode pitch of the M4PP measurements (4-12 μm). Within the limits of the used analysis and the investigated range, this film can thus be said to be electrically continuous.

It is not reasonable to extend our results to the point of predicting the electrical continuity of CVD grown graphene on Cu foils or Cu single crystals in general. There are numerous reports on high quality graphene in literature grown on Cu single crystals[12–14] as well as Cu foils[58,59], including observations of Drude-like THz responses in studies of CVD graphene grown on Cu foils[26–28]. The keypoint of this work is a method of detecting the presence (or absence) of extended defects on different length scales in a way that directly relates to impact on the conducting properties, which can be extended to large areas of graphene. Due to the non-contact nature and fast acquisition rate of the technique, THz-TDS analysis can realistically be applied

to arbitrarily large films in industrial settings, and as the quality and mobility of synthesized large-area graphene increases, a lower frequency range is required to accurately discern between the continuous (Drude) and semi- or dis-continuous (Drude-Smith) regimes, making this type of analysis approachable with simpler systems that offer much higher throughput. The M4PP approach is routinely applied in the semiconductor industry using commercially available equipment that meets the demands of the silicon industry for reliability, cleanliness, and throughput. Although electrical continuity is obviously of crucial importance judging from the widespread concerns for cracks and tears in the literature on transfer methods[60,61], we believe this work is first to propose a systematic, quantitative approach to evaluate the actual electrical continuity, addressing the question of whether a graphene film is truly electrically two-dimensional or not on multiple scales.

In summary, we show how the electrical continuity of CVD graphene may be evaluated by ultra-broadband THz-TDS and dual configuration M4PP conductance mapping across several orders of magnitude in length scale from approximately 100 nm to 10 μm. In particular, we verify that CVD graphene grown on SC Cu and transferred without damaging neither the catalyst nor the graphene using an electrochemical delamination method, indeed shows clear, unambiguous signatures of continuous, two-dimensional electrical conduction on the nano-, micro-, as well as intermediate length scale. This stands in stark contrast to present and prior observations of electrical discontinuity in CVD graphene grown on CF Cu. Ultra-broadband THz-TDS measurements show that while the conductance spectrum of graphene grown on SC Cu closely follows the Drude model which describes a two-dimensional conductor without backscattering on the nanoscopic scale, graphene grown on CF Cu presents characteristic signatures of nanoscopic preferential backscattering, accurately reproduced by the Drude-Smith model. Such features are commonly interpreted to be the consequence of extended, semi-insulating defects, which in the present context, suggests that back-scattering on domain boundaries or wrinkles in this graphene is significant. Dual configuration M4PP measurements distinguish the electrical response of continuous graphene from that of graphene with extended defects on the few-micron scale, as defined by the electrode pitch. Comparisons of resistance measurements in two different current-voltage configurations show that SC Cu grown CVD graphene exhibits distinctive traits of continuous two-dimensional electronic transport on the microscopic scale, which is not the case for the two CF Cu grown samples. Finally, we have verified the electrical continuity of SC Cu grown CVD graphene on intermediate length scales through a direct comparison of nanosopic and microscopic sheet conductance. Extended defects occurring on an intermediate length scale will intuitively lead to reduced conductance measured by M4PP compared to that measured by THz-TDS, as M4PP measurements interrogate the graphene films on a much larger length scale. A direct comparison of thousands of measurement points show that the correlation of M4PP to THz-TDS sheet conductance for CF Cu grown samples is significantly below 1:1, while graphene grown on SC Cu shows a correlation much closer to unity, revealing that graphene from SC Cu has a significantly higher degree of continuity on the intermediate scale between the probing length scales of the two applied methods.

Acknowledgements

The Danish National Research Foundation has funded both Center for Individual Nanoparticle Functionality (CINF)(DNRF54) and Center for Nanostructured Graphene (CNG)(DNRF58). This work was supported by Villum Foundation, project. No. VKR023117.

References

(1) Novoselov, K. S.; Geim, A. K. K.; Morozov, S. V. V; Jiang, D.; Zhang, Y.; Dubonos, S. V. V; Grigorieva, I. V. V; Firsov, A. A. A. *Science (80-.).* **2004**, *306*, 666–669.

(2) Kim, K. S.; Zhao, Y.; Jang, H.; Lee, S. Y.; Kim, J. M.; Kim, K. S.; Ahn, J.-H.; Kim, P.; Choi, J.-Y.; Hong, B. H. *Nature* **2009**, *457*, 706–710.

(3) Li, X.; Cai, W.; An, J.; Kim, S.; Nah, J.; Yang, D.; Piner, R.; Velamakanni, A.; Jung, I.; Tutuc, E.; Banerjee, S. K.; Colombo, L.; Ruoff, R. S. *Science (80-.).* **2009**, *324*, 1312 –1314.

(4) Wang, L.; Meric, I.; Huang, P. Y.; Gao, Q.; Gao, Y.; Tran, H.; Taniguchi, T.; Watanabe, K.; Campos, L. M.; Muller, D. A.; Guo, J.; Kim, P.; Hone, J.; Shepard, K. L.; Dean, C. R. *Science* **2013**, *342*, 614–617.

(5) Ajayan, P. M.; Yakobson, B. I. *Nat. Mater.* **2011**, *10*, 415–417.

(6) Lotz, M. R.; Boll, M.; Hansen, O.; Kjær, D.; Bøggild, P.; Petersen, D. H. *Appl. Phys. Lett.* **2014**, *Accepted f.*

(7) Tsen, A. W.; Brown, L.; Levendorf, M. P.; Ghahari, F.; Huang, P. Y.; Havener, R. W.; Ruiz-Vargas, C. S.; Muller, D. A.; Kim, P.; Park, J. *Science* **2012**, *336*, 1143–1146.

(8) Yu, Q.; Jauregui, L. A.; Wu, W.; Colby, R.; Tian, J.; Su, Z.; Cao, H.; Liu, Z.; Pandey, D.; Wei, D.; Chung, T. F.; Peng, P.; Guisinger, N. P.; Stach, E. A.; Bao, J.; Pei, S.-S.; Chen, Y. P. *Nat. Mater.* **2011**, *10*, 443–449.

(9) Kholmanov, I. N.; Magnuson, C. W.; Aliev, A. E.; Li, H.; Zhang, B.; Suk, J. W.; Zhang, L. L.; Peng, E.; Mousavi, S. H.; Khanikaev, A. B.; Piner, R.; Shvets, G.; Ruoff, R. S. *Nano Lett.* **2012**, *12*, 5679–5683.

(10) Radchenko, T. M.; Shylau, A. A.; Zozoulenko, I. V.; Ferreira, A. *Phys. Rev. B* **2013**, *87*, 195448.

(11) Petrone, N.; Meric, I.; Hone, J.; Shepard, K. L. *Nano Lett.* **2013**, *13*, 121–125.

(12) Ago, H.; Kawahara, K.; Ogawa, Y.; Tanoue, S.; Bissett, M. A.; Tsuji, M.; Sakaguchi, H.; Koch, R. J.; Fromm, F.; Seyller, T.; Komatsu, K.; Tsukagoshi, K. *Appl. Phys. Express* **2013**, *6*, 075101.

(13) Miller, D. L.; Keller, M. W.; Shaw, J. M.; Rice, K. P.; Keller, R. R.; Diederichsen, K. M. *AIP Adv.* **2013**, *3*, 082105.

(14) Tao, L.; Lee, J.; Holt, M.; Chou, H.; McDonnell, S. J.; Ferrer, D. A.; Babenco, M. G.; Wallace, R. M.; Banerjee, S. K.; Ruoff, R. S.; Akinwande, D. *J. Phys. Chem. C* **2012**, *116*, 24068–24074.

(15) Rasool, H. I.; Song, E. B.; Mecklenburg, M.; Regan, B. C.; Wang, K. L.; Weiller, B. H.; Gimzewski, J. K. *J. Am. Chem. Soc.* **2011**, *133*, 12536–12543.

(16) Wang, Y.; Zheng, Y.; Xu, X.; Dubuisson, E.; Bao, Q.; Lu, J.; Loh, K. P. *ACS Nano* **2011**, *5*, 9927–9933.

(17) Li, J.; Zhang, S.-L. *Phys. Rev. E* **2009**, *80*, 040104.

(18) Walther, M.; Cooke, D. G.; Sherstan, C.; Hajar, M.; Freeman, M. R.; Hegmann, F. A. *Phys. Rev. B* **2007**, *76*, 125408.

(19) Buron, J. D.; Petersen, D. H.; Bøggild, P.; Cooke, D. G.; Hilke, M.; Sun, J.; Whiteway, E.; Nielsen, P. F.; Hansen, O.; Yurgens, A.; Jepsen, P. U. *Nano Lett.* **2012**, *12*, 5074–5081.

(20) Turner, G. M.; Beard, M. C.; Schmuttenmaer, C. A. *J. Phys. Chem. B* **2002**, *106*, 11716–11719.

(21) Cooke, D. G.; MacDonald, A. N.; Hryciw, A.; Wang, J.; Li, Q.; Meldrum, A.; Hegmann, F. A. *Phys. Rev. B* **2006**, *73*, 193311.

(22) Cooke, D. G.; Meldrum, A.; Uhd Jepsen, P. *Appl. Phys. Lett.* **2012**, *101*, 211107.

(23) Cooke, D. G.; Krebs, F. C.; Jepsen, P. U. *Phys. Rev. Lett.* **2012**, *108*, 056603.

(24) Dawlaty, J. M.; Shivaraman, S.; Strait, J.; George, P.; Chandrashekhar, M.; Rana, F.; Spencer, M. G.; Veksler, D.; Chen, Y. *Appl. Phys. Lett.* **2008**, *93*, 131905–131905–3.

(25) Choi, H.; Borondics, F.; Siegel, D. A.; Zhou, S. Y.; Martin, M. C.; Lanzara, A.; Kaindl, R. A. *Appl. Phys. Lett.* **2009**, *94*, 172102.

(26) Horng, J.; Chen, C.-F.; Geng, B.; Girit, C.; Zhang, Y.; Hao, Z.; Bechtel, H. A.; Martin, M.; Zettl, A.; Crommie, M. F.; Shen, Y. R.; Wang, F. *Phys. Rev. B* **2011**, *83*, 165113.

(27) Ren, L.; Zhang, Q.; Yao, J.; Sun, Z.; Kaneko, R.; Yan, Z.; Nanot, S.; Jin, Z.; Kawayama, I.; Tonouchi, M.; Tour, J. M.; Kono, J. *Nano Lett.* **2012**, *12*, 3711–3715.

(28) Jnawali, G.; Rao, Y.; Yan, H.; Heinz, T. F. *Nano Lett.* **2013**, *13*, 524–530.

(29) Ni, Z. H.; Wang, H. M.; Kasim, J.; Fan, H. M.; Yu, T.; Wu, Y. H.; Feng, Y. P.; Shen, Z. X. *Nano Lett.* **2007**, *7*, 2758–2763.

(30) Cook, D. J.; Hochstrasser, R. M. *Opt. Lett.* **2000**, *25*, 1210.

(31) Kress, M.; Löffler, T.; Eden, S.; Thomson, M.; Roskos, H. G. *Opt. Lett.* **2004**, *29*, 1120.

(32) Xie, X.; Dai, J.; Zhang, X.-C. *Phys. Rev. Lett.* **2006**, *96*, 075005.

(33) Dai, J.; Xie, X.; Zhang, X.-C. *Phys. Rev. Lett.* **2006**, *97*.

(34) Karpowicz, N.; Dai, J.; Lu, X.; Chen, Y.; Yamaguchi, M.; Zhao, H.; Zhang, X.-C.; Zhang, L.; Zhang, C.; Price-Gallagher, M.; Fletcher, C.; Mamer, O.; Lesimple, A.; Johnson, K. *Appl. Phys. Lett.* **2008**, *92*, 011131.

(35) Klarskov, P.; Strikwerda, A. C.; Iwaszczuk, K.; Jepsen, P. U. *New J. Phys.* **2013**, *15*, 075012.

(36) Zalkovskij, M.; Zoffmann Bisgaard, C.; Novitsky, A.; Malureanu, R.; Savastru, D.; Popescu, A.; Uhd Jepsen, P.; Lavrinenko, A. V. *Appl. Phys. Lett.* **2012**, *100*, 031901.

(37) Jeon, T.-I.; Grischkowsky, D. *Appl. Phys. Lett.* **1998**, *72*, 3032.

(38) Petersen, D. H.; Hansen, O.; Hansen, T. M.; Petersen, P. R. E.; Bøggild, P. *Microelectron. Eng.* **2008**, *85*, 1092–1095.

(39) Wang, F.; Petersen, D. H.; Jensen, H. V.; Hansen, C.; Mortensen, D.; Friis, L.; Hansen, O. *J. Micromechanics Microengineering* **2011**, *21*.

(40) Rymaszewski, R. *J. Phys. E.* **1969**, *2*, 170–174.

(41) Thorsteinsson, S.; Wang, F.; Petersen, D. H.; Hansen, T. M.; Kjær, D.; Lin, R.; Kim, J.-Y.; Nielsen, P. F.; Hansen, O. *Rev. Sci. Instrum.* **2009**, *80*, 53902–53910.

(42) Koon, D. W.; Knickerbocker, C. J. *Rev. Sci. Instrum.* **1992**, *63*, 207–210.

(43) Náhlík, J.; Kašpárková, I.; Fitl, P. *Measurement* **2011**, *44*, 1968–1979.

(44) Koon, D. W. *Rev. Sci. Instrum.* **2006**, *77*, 094703.

(45) Klarskov, M. B.; Dam, H. F.; Petersen, D. H.; Hansen, T. M.; Löwenborg, A.; Booth, T. J.; Schmidt, M. S.; Lin, R.; Nielsen, P. F.; Bøggild, P. *Nanotechnology* **2011**, *22*, 445702.

(46) Ferrari, A. C. *Solid State Commun.* **2007**, *143*, 47–57.

(47) Ferrari, A. C.; Meyer, J. C.; Scardaci, V.; Casiraghi, C.; Lazzeri, M.; Mauri, F.; Piscanec, S.; Jiang, D.; Novoselov, K. S.; Roth, S.; Geim, A. K. *Phys. Rev. Lett.* **2006**, *97*, 187401.

(48) Cançado, L. G.; Jorio, A.; Ferreira, E. H. M.; Stavale, F.; Achete, C. A.; Capaz, R. B.; Moutinho, M. V. O.; Lombardo, A.; Kulmala, T. S.; Ferrari, A. C. *Nano Lett.* **2011**, *11*, 3190–3196.

(49) Das Sarma, S.; Adam, S.; Hwang, E. H.; Rossi, E. *Rev. Mod. Phys.* **2011**, *83*, 407–470.

(50) Hwang, E.; Adam, S.; Sarma, S. *Phys. Rev. Lett.* **2007**, *98*, 186806.

(51) Castro Neto, A. H.; Peres, N. M. R.; Novoselov, K. S.; Geim, A. K. *Rev. Mod. Phys.* **2009**, *81*, 109–162.

(52) Nomura, K.; MacDonald, A. H. *Phys. Rev. Lett.* **2007**, *98*, 076602.

(53) Dadrasnia, E.; Lamela, H.; Kuppam, M. B.; Garet, F.; Coutaz, J.-L. *Adv. Condens. Matter Phys.* **2014**, *2014*.

(54) Smith, N. V. *Phys. Rev. B* **2001**, *64*, 155106.

(55) Němec, H.; Kužel, P.; Sundström, V. *Phys. Rev. B* **2009**, *79*, 115309.

(56) Titova, L. V.; Cocker, T. L.; Cooke, D. G.; Wang, X.; Meldrum, A.; Hegmann, F. A. *Phys. Rev. B* **2011**, *83*, 085403.

(57) Petersen, D. H.; Lin, R.; Hansen, T. M.; Rosseel, E.; Vandervorst, W.; Markvardsen, C.; Kjær, D.; Nielsen, P. F. *J. Vac. Sci. Technol. B Microelectron. Nanom. Struct.* **2008**, *26*, 362.

(58) Petrone, N.; Dean, C. R.; Meric, I.; van der Zande, A. M.; Huang, P. Y.; Wang, L.; Muller, D.; Shepard, K. L.; Hone, J. *Nano Lett.* **2012**, *12*, 2751–2756.

(59) Hao, Y.; Bharathi, M. S.; Wang, L.; Liu, Y.; Chen, H.; Nie, S.; Wang, X.; Chou, H.; Tan, C.; Fallahazad, B.; Ramanarayan, H.; Magnuson, C. W.; Tutuc, E.; Yakobson, B. I.; McCarty, K. F.; Zhang, Y.-W.; Kim, P.; Hone, J.; Colombo, L.; Ruoff, R. S. *Science* **2013**, *342*, 720–723.

(60) Liang, X.; Sperling, B. A.; Calizo, I.; Cheng, G.; Hacker, C. A.; Zhang, Q.; Obeng, Y.; Yan, K.; Peng, H.; Li, Q.; Zhu, X.; Yuan, H.; Walker, A. R. H.; Liu, Z.; Peng, L.-M.; Richter, C. A. *ACS Nano* **2011**, *5*, 9144–9153.

(61) Suk, J. W.; Kitt, A.; Magnuson, C. W.; Hao, Y.; Ahmed, S.; An, J.; Swan, A. K.; Goldberg, B. B.; Ruoff, R. S. *ACS Nano* **2011**, *5*, 6916–6924.